

Full Length Article

# Intrinsic cellular instabilities of hydrogen laminar outwardly propagating spherical flames

Yu Xie<sup>a</sup>, Mohamed Elsayed Morsy<sup>a,b</sup>, Jinzhou Li<sup>a</sup>, Junfeng Yang<sup>a,\*</sup>

<sup>a</sup> School of Mechanical Engineering, University of Leeds, Leeds LS2 9JT, United Kingdom

<sup>b</sup> Faculty of Engineering at El-Mattaria, University of Helwan, Cairo 11718, Egypt



## ARTICLE INFO

**Keywords:**  
Laminar premixed flames  
Onset of cellularity  
Hydrogen  
Instabilities

## ABSTRACT

In this study, the influences of pressure, temperature and equivalence ratio on the onset of cellular instabilities in premixed hydrogen/air laminar flames were studied using a constant volume fan-stirred combustion vessel. The onset of instability is marked by the critical stretch rate, at which the flame speed rapidly deviates from its prior response to stretch. It is noted that the critical Peclet number,  $Pe_{cl}$ , increases with increasing both equivalence ratio and temperature, indicating a more stable flame. Whilst,  $Pe_{cl}$  decreases with increasing the initial pressure due to the associated decrease in the flame speed Markstein number,  $Ma_b$ , with increasing pressure. Empirical correlations of  $Pe_{cl}$  and  $K_{cl}$ , as a function of  $Ma_b$ , pressure, temperature, and equivalence ratio are developed and presented. Such correlations can be employed to estimate the severity of large-scale atmospheric hydrogen flames.

## 1. Introduction

Cellular instability and self-acceleration of premixed flames are commonly observed in fuel combustion, and are governed by the thermal-diffusive and hydrodynamic instability. Studying the hydrogen flame instability and mapping its stable regime have the practice interest when designing energy-efficient combustors (e.g. hydrogen engines, domestic burners and gas turbines) and investigating hydrogen explosion hazards. Laminar combustion plays an essential role in the study of the combustion process because it consists of indispensable information in regard to the reactivity, diffusivity, and exothermicity of a combustible mixture. Laminar burning velocity and intrinsic instabilities have been commonly considered as the two most significant and crucial aspects [1,2].

In the propagation of a laminar premixed flame, the inherent flame front instability and the spontaneous formation of cells through hydrodynamic, Darrieus–Landau (D-L) and thermal diffusion instabilities are often experimentally observed [3,4]. The buoyancy instability induced by gravity has also been reported in the previous work [5]. This tends to be ignored because of its negligible effect on rapidly propagating flames compared to the first two types of instabilities. In the initial stage of flame development, the folds at the flame front are dominated by small-scale thermal diffusion instability. As the flame grows, the flame radius

becomes much larger than the flame thickness, and D-L instability gradually dominates the flame morphology and accelerative dynamics [6].

Local unstable flame morphology induced by D-L and thermal diffusion instabilities correspondingly affects the local heat release rate, combustion efficiency and emissions. Hydrogen-air laminar combustion has been investigated widely in the past few decades. Faeth et al. [7,8] studied the conditions incurring the instability of hydrogen-air flames and categorized three kinds of instabilities which have the most significant effects. Several studies [9,10] have shown that initial pressure ( $P_i$ ), initial temperature ( $T_i$ ) and equivalence ratio ( $\phi$ ) are the main parameters affecting flame instability. Bradley et al. [1,11], Hu et al. [12] and Huo et al. [13,14] further studied the formation schemes of cellular flame structures, the critical radius and the Peclet number in the process of spherical hydrogen flame propagation.

To quantify the onset of cellular instability, critical Peclet number,  $Pe_{cl}$ , defined as critical radius,  $r_{cl}$ , normalised by flame thickness,  $\delta$ , have been studied extensively [15]. Bechtold and Matlon [2] evaluated  $Pe_{cl}$  considering hydrodynamic and thermal diffusion effects. The linear instability peninsula based on dimensionless groups was firstly presented for spherically expanding flames using critical Peclet number. For hydrocarbon fuels, it has been concluded that  $Pe_{cl}$  decreases with the increase of  $\phi$  [16,17]. However, for hydrogen-air combustion, the trend of  $Pe_{cl}$  increases due to the opposite trend in thermal diffusion instability

\* Corresponding author.

E-mail address: [J.Yang@leeds.ac.uk](mailto:J.Yang@leeds.ac.uk) (J. Yang).

<https://doi.org/10.1016/j.fuel.2022.125149>

Received 23 February 2022; Received in revised form 29 June 2022; Accepted 29 June 2022

Available online 6 July 2022

0016-2361/© 2022 The Author(s). Published by Elsevier Ltd. This is an open access article under the CC BY license (<http://creativecommons.org/licenses/by/4.0/>).

**Nomenclature**

$A$	laminar flame surface area ( $\text{m}^2$ )
$c_p$	specific heat ( $\text{J}/(\text{kg}\cdot\text{K})$ )
$F$	flame speed enhancement factor, the ratio of flame speeds with and without instabilities $S_n/S$
$k$	thermal conductivity ( $\text{W}/(\text{m}\cdot\text{K})$ )
$K_{cl}$	critical laminar Karlovitz number
$K_{cl,0}$	datum value of $K_{cl}$ at $T_0$ and $P_0$
$L$	Markstein length (mm)
$L_b$	flame speed Markstein length (mm)
$Le$	Lewis number
$Ma$	Markstein number
$Ma_b$	burned gas Markstein number
$Ma_{sr}$	Markstein number associated to aerodynamic strain
$Ma_{cr}$	Markstein number associated to flame curvature
$n_l$	smallest unstable wavenumber
$n_{l,cl}$	$n_l$ at critical flame radius
$Pe$	Peclet number
$Pe_{cl}$	critical Peclet number
$Pe_{cl,0}$	datum value of $Pe_{cl}$ at $T_0$ and $P_0$
$P_i$	initial pressure (MPa)
$P_0$	datum atmospheric pressure (0.1 MPa)
$r_{cl}$	critical flame radius (mm)
$r_u$	cold flame radius (mm)
$r_{cl,0}$	datum value of $r_{cl}$ at $T_0$ and $P_0$
$R_{sch}$	front radius obtained by Schlieren ciné-photography (mm)
$S$	theoretical flame speed without instability (m/s)

$S_n$	stretched flame speed (m/s)
$S_s$	flame speed at zero stretch rate (m/s)
$T_i$	initial temperature (K)
$T^0$	inner layer temperature (K)
$T_0$	datum atmospheric temperature (300 K)
$u_l$	unstretched laminar burning velocity (m/s)
$u_{nr}$	stretched laminar mass burning velocity expressing mass burning rate (m/s)

**Greek symbols**

$\alpha$	flame stretch rate (1/s)
$\alpha_{cl}$	critical flame stretch rate (1/s)
$\alpha_r, \alpha_p, \alpha_k$	temperature coefficients for $r_{cl}, Pe_{cl}, K_{cl}$
$\beta_r, \beta_p, \beta_k$	pressure coefficients for $r_{cl}, Pe_{cl}, K_{cl}$
$\gamma_r, \gamma_p, \gamma_k$	equivalence ratio coefficients for $r_{cl}, Pe_{cl}, K_{cl}$
$\delta$	flame thickness (mm)
$\delta_l$	simplistic laminar flame thickness (mm) $\nu/u_l$
$\delta_k$	preheat zone flame thickness (mm) $(k/C_p)_{T^0}/(\rho_u u_l)$
$\delta_D$	flame thickness based on mass diffusivity divided by laminar burning velocity (mm)
$\delta_T$	flame thickness, using temperature gradient method (mm) $(T_{ad} - T_u)/(dT/dx)_{\max}$
$\nu$	unburnt gas kinematic viscosity ( $\text{m}^2/\text{s}$ )
$\rho_u$	unburnt gas density ( $\text{kg}/\text{m}^3$ )
$\sigma$	ratio of unburned gas density to burned gas density
$\phi$	equivalence ratio
$\phi_0$	datum equivalence ratio (1)

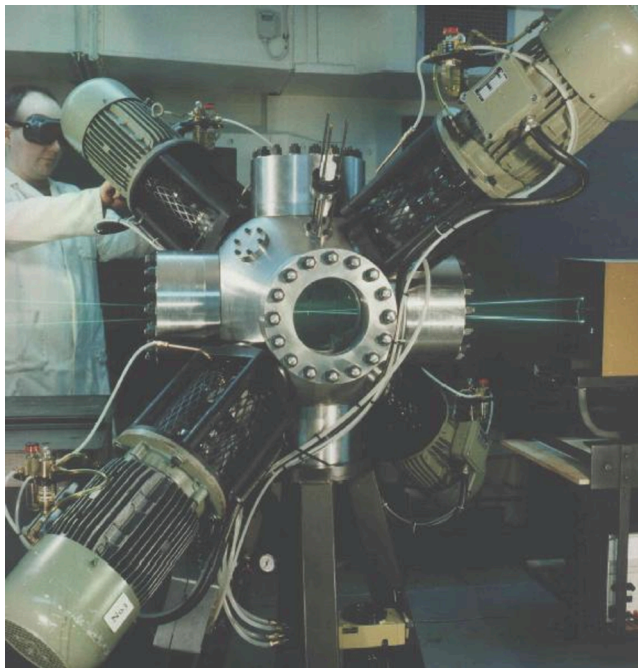


Fig. 1. Leeds MKII fan-stirred vessel [28].

with  $\phi$  [18,19].  $Pe_{cl}$  is also affected by  $P_i$  associated with respect to the hydrodynamic effects. The evaluated  $Pe_{cl}$  is usually correlated with Markstein number,  $Ma$ , presented as Markstein length,  $L$ , normalized by  $\delta$ , and the critical point at which the instability starts is still an important topic of current research. In particular, it is important to study the flame instability and its subsequent effects on the acceleration of flame speed

[13]. Different empirical correlations of  $Pe_{cl}$  with respect to  $Ma$  have been proposed for various fuels [20–24]. They all show a moderate agreement in terms of increasing trend for  $Pe_{cl}$ . However, the coefficients of the correlations vary significantly, which may be attributed to the different definitions and selections of  $r_{cl}$  and the uncertainty of  $Ma$  for hydrogen. Despite the enormous efforts have been addressed on the onset of flame instability in the past decades, no consensus on these correlations has been achieved yet.

Critical laminar Karlovitz number,  $K_{cl}$ , associated with the critical flame stretch rate,  $\alpha_{cl}$ , multiplied by the chemical time,  $\delta/u_l$ , is considered a more relevant parameter than  $Pe_{cl}$  because the former can better define the onset of instability [25] as a function of the fundamental parameter, stretch rate. Valid data and correlations of  $K_{cl}$  for hydrogen-air flames at a wide range of conditions are scarce. Moreover, quantifications of  $Pe_{cl}$  and  $K_{cl}$  are based on the flame thickness which are often defined by  $\delta_l \cong k/\rho_u c_p u_l \cong \nu/u_l$  [11] or temperature gradient method [19]. However, these approximations are invalid for hydrogen/air flames because of the rapid diffusion of  $H$  atoms towards the leading edge, and the much reduced preheat zone compared with hydrocarbon flames. Lewis numbers ( $Le$ ) of hydrogen and hydrocarbons (e.g. methane, *iso*-octane) have the opposite trend with the increase of  $\phi$  [10]. Much work on these critical dimensionless number have been undertaken with hydrocarbon fuels. The dependencies of  $Pe_{cl}$ ,  $K_{cl}$  on pressure and Markstein number were reported for 9 different fuels based on the classical flame thickness [26]. The results showed a wide divergence of hydrogen from the other hydrocarbon data. Consequently, the former quantifications of  $Pe_{cl}$ ,  $K_{cl}$  and the correlations of the dependency of  $Pe_{cl}$ ,  $K_{cl}$  on Markstein number for hydrogen must be revisited and improved. In addition, it is well known that the initial conditions, e.g.  $T_i$ ,  $P_i$  and  $\phi$  determine the onset of cellularity of stable flames. Therefore, it is worthwhile to develop a prediction model for the cellularity onset of the hydrogen flames.

Owing to such considerations, the objectives of the present study are: (i) to provide experimental combustion characteristics data (laminar

burning velocities, burned gas Markstein number, reasonable hydrogen flame thickness) for hydrogen over a wide range of initial conditions; (ii) to define the stable regime for the propagation of hydrogen based on the dependences of  $r_{cl}$ ,  $Pe_{cl}$ , and  $K_{cl}$  on  $Ma$ , and develop related correlations; (iii) to develop an updated method for accurate predictions of the onset of flame instability and to introduce new correlations of  $r_{cl}$ ,  $Pe_{cl}$ , and  $K_{cl}$  with respect to the initial conditions, e.g.  $P_i$ ,  $T_i$  and  $\phi$ .

The rest of this paper is organized as follows. In Section 2, the experimental setup is introduced, whilst the data processing methodology is described in Section 3. Results and discussions are presented in Section 4, including flame topography, flame characteristics and prediction models for hydrogen flame instability. Finally, Section 5 is devoted to concluding remarks.

## 2. Experimental apparatus

A 380-mm-diameter spherical stainless-steel vessel capable of withstanding  $P_i$  of up to 1.5 MPa and  $T_i$  of up to 600 K, with extensive optical access through three pairs of orthogonal windows of 150 mm diameter, was employed as shown in Fig. 1[27,28]. The vessel was equipped with four fans driven by electric motors, which were used solely to ensure the reactants were well mixed before ignition in the present work. Two electric heaters (2 kW) were connected to the inside wall of the vessel for preheating the vessel and air-fuel mixture to meet the requirements. The gas temperature was measured by a sheathed chromel-alumel thermocouple. Pressures were measured during an explosion with a Kistler pressure transducer. A central spark plug was used with minimum ignition energies of about 1 mJ, which was supplied from a 12 V transistorized automotive ignition coil. This energy is the discharge energy from the secondary circuit of the ignition coil [29]. Flame images were captured by adopting a Schlieren ciné-photography system (light source provided by a MI-150 Fiber Optic Illuminator, 220 V) combined with the MATLAB code to analyze flame characteristics, including flame radius, flame speed, stretch rate,  $Ma$ ,  $Pe$ . A high-speed camera (SpeedSense 2640, DANTEC DYNAMICS Co., Ltd, UK) was used for image acquisition at 30 000 fps and 768×768 pixels (0.263 mm/pixel resolution). More details about the vessel and its auxiliary systems are in [28].

In the experiments, the hydrogen with 99.995% purity was employed, and the air was composed of industrial oxygen and industrial nitrogen with the ratio of 21:79 % by mol. The equivalence ratio,  $\phi$ , was set as 0.4, 0.5, 0.6, 0.7, 0.8, 0.9, 1.0, 1.2, 1.5 and 2.  $P_i$  was set as 0.1, 0.3 and 0.5 MPa, and  $T_i$  was set as 300, 360 and 400 K in this study. The experimental repeatability was checked through three realizations at each experimental condition. Average values from sets of three experiments were used, to increase the certainty of our measurements. The standard deviation error bar was defined to be the square root of the variance (a sum of squared deviation divided by the number of data points, 3, for each test condition). The error bars were plotted around the mean values in all experimental results.

## 3. Data processing method

For an outwardly propagating spherical flame, the total stretch rate at the cold front of the flame is:

$$\alpha = \frac{1}{A} \frac{dA}{dt} = \frac{2}{r_u} \frac{dr_u}{dt} = \frac{2}{r_u} S_n \quad (1)$$

where  $A$  is the laminar flame surface area. The stretched flame speed,  $S_n$  is calculated from the evolution of the cold flame radius (5 K above the temperature of the reactants),  $r_u$ , with time as  $S_n = dr_u/dt$ .  $r_u$  is calculated from the front radius defined in Schlieren ciné-photography ( $R_{sch}$ ) [21].

A linear model is adopted here to depict the relationship between  $S_n$  and  $\alpha$  given by:

$$S_s - S_n = L_b \alpha \quad (2)$$

Here  $S_s$  is the flame speed at zero stretch rate. The equation yields values of Markstein length of flame speed,  $L_b$ , which can be normalized with respect to the flame thickness to yield burned gas side Markstein number  $Ma_b$ . Additionally,  $Ma_{sr}$  and  $Ma_{cr}$  are the Markstein numbers associated with the strain and curvature stretch rates, respectively.

The curve of  $S_n$  was plotted against the flame stretch rate,  $\alpha$  by extrapolating the linear fitting line to the stretch rate of 0, unstretched flame speed  $S_s$  was obtained as the intercept, which represents the theoretical burning velocity without any stretch rate. The unstretched flame speed could not be measured directly but it was deduced from Eq. (2). However, it is an indispensable parameter to calculate the unstretched laminar burning velocity:

$$u_l = S_s \frac{\rho_b}{\rho_u} \quad (3)$$

According to the nonlinear asymptotic theory, a nonlinear relationship of  $S_n$  and  $\alpha$  proposed by Kelley and Law [30,31] was adopted here for the purpose of comparison with the linear extrapolation method.

$$\left(\frac{S_n}{S_s}\right)^2 \ln\left(\frac{S_n}{S_s}\right)^2 = -2 \frac{L_b \alpha}{S_s} \quad (4)$$

Laminar flame thickness has been defined by various methods [20]. The laminar flame thickness,  $\delta$ , defined as the distance between the burned zone and unburned zone, is a parameter governing the intensity of hydrodynamic instability. Many researchers used the simplistic expressions for  $\delta_l$ , which can be an approximate guide to the flame thickness[11]:

$$\delta_l \cong \frac{\nu}{u_l} \quad (5)$$

where  $\nu$  is the unburnt gas kinematic viscosity.

Following the temperature profile across a premixed laminar flame, the flame thickness can be identified directly by seeking the distance from where the extended tangent meets the unburned fuel temperature, and the combustion products temperature [19], expressed as:

$$\delta_T = (T_{ad} - T_u)/(dT/dx)_{\max} \quad (6)$$

where  $(dT/dx)_{\max}$  is the maximum temperature gradient.

This definition of the flame thickness can be only used with flames of the chemically inert preheat zone. For methane, propane, ethylene, and acetylene flames, this definition could readily be linked to the classical definition of the flame thickness that uses the  $X$ -interval spanned by the steepest tangent to the temperature profile between the unburnt and adiabatic temperature as the flame thickness. However, the applicability of the traditional equation for hydrogen flames becomes questionable since the underlying assumption of a chemically inert preheat zone does not exist here.  $H$  atoms diffuse rapidly in laminar flames towards the leading edge, where they initiate reaction to a greater extent than in hydrocarbon flames, the preheat zone is much reduced. Hence, the specified method for calculating flame thickness, preheat zone flame thickness,  $\delta_k$ , is obtained from the following expression [32]:

$$\delta_k = \frac{(k/c_p)_{T^0}}{\rho_u u_l} \quad (7)$$

where  $(k/c_p)_{T^0}$  is the ratio of thermal conductivity and specific heat at a certain inner layer temperature,  $T^0$ . The values of  $T^0$  for different gases are presented in [32].

During the laminar flame expansion, two instants with non-smooth flame surfaces were observed: first, the continuous formation of large cracks along with its branch, non-uniformity of the local unburned mixture, non-ignorable and un-even distribution of spark energy and unequal diffusion instability can account for this; second, the sudden and spontaneous emergence of the majority of crystal cell structures over the full flame surface. The characteristic length scales of these cells

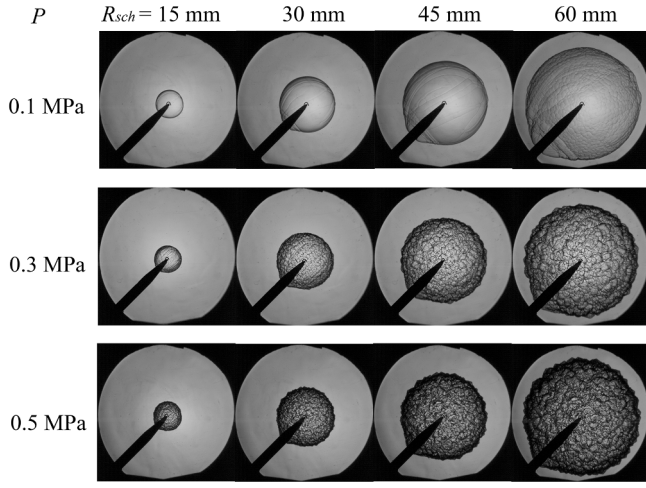


Fig. 2. Schlieren images showing the impact of  $P_i$  on the expanding hydrogen-air flames at  $P_i = 0.1, 0.3$  and  $0.5$  MPa,  $T_i = 360$  K,  $\phi = 0.8$ .

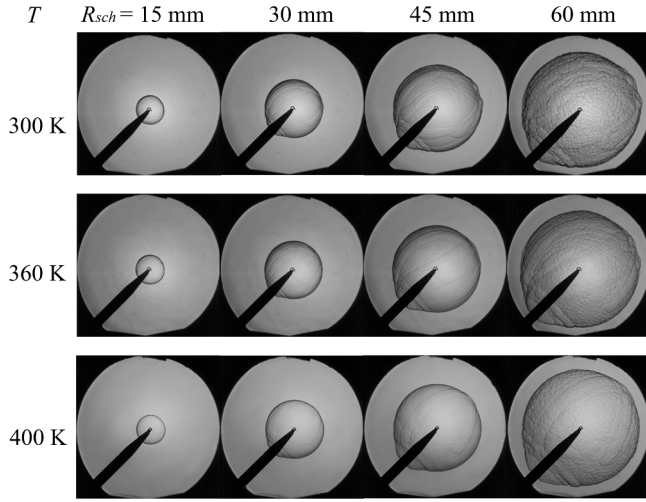


Fig. 3. Schlieren images showing the impact of  $T_i$  on the expanding hydrogen-air flames at  $T_i = 300, 360$  and  $400$  K,  $P_i = 0.1$  MPa,  $\phi = 0.8$ .

were quite small compared to that of large cracks. The hydrodynamic instability is responsible for the appearance of such cells. In conclusion, the second instant is regarded as the onset of flame instability in this study. The reason being: firstly, hydrodynamic instability exists in almost all flame propagation, but non-uniform diffusion instability is not. Secondly, compared with the slow progressive growth and branching of large cracks, the intensity of hydrodynamic instability is very high, which means that tiny cells grow on the whole flame surface.

A key parameter is the critical flame radius,  $r_{cl}$ , the flame radius at which the cellular flame structure becomes apparent (the second instant). The appropriate dimensionless radius is critical Peclet number,  $Pe_{cl}$ , as:

$$Pe_{cl} = \frac{r_{cl}}{\delta} \quad (8)$$

The onset of cell formation at  $Pe_{cl}$  presents the dimensionless critical radius of the onset of cellularity due to the limiting stretch rate, which also is a convenient measurable parameter.  $Pe_{cl}$  and cellularity are closely linked and appear at the same time, but  $Pe_{cl}$  is not the fundamental reason for cellularity. Since the flame is stabilised by the stretch, a laminar critical Karlovitz number,  $K_{cl}$ , expressed on the basis of the critical total flame stretch rate,  $\alpha_{cl}$ , is introduced to reveal the intrinsic nature of the flame instability:

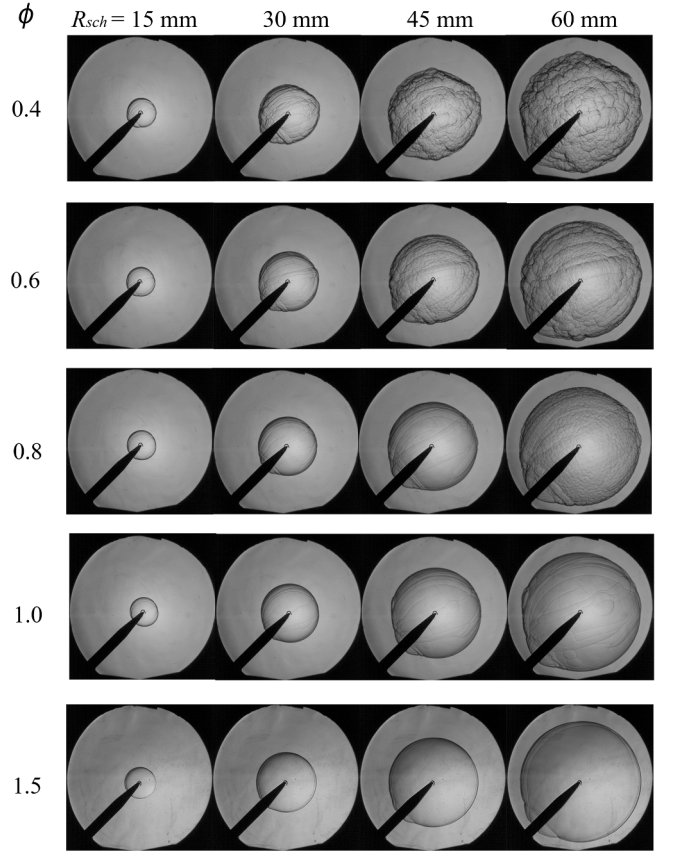


Fig. 4. Schlieren images showing the impact of  $\phi$  on the expanding hydrogen-air flames at  $\phi = 0.4, 0.6, 0.8, 1.0, 1.5$ ,  $T_i = 360$  K,  $P_i = 0.1$  MPa.

$$K_{cl} = \alpha_{cl} \frac{\delta}{u_l} \quad (9)$$

Then  $K_{cl}$  can be derived as follows [26]:

$$K_{cl} = (2\sigma/Pe_{cl})[1 + (2Ma_b/Pe_{cl})]^{-1} \quad (10)$$

where  $\sigma$  is the ratio of unburned gas density to burned gas density.

According to the linear instability theory of Bechtold and Matalon [2] and the fractal theory [15], a flame speed enhancement factor,  $F$ , the ratio of flame speeds with and without instabilities,  $S_n$  and  $S$  [11] was proposed to handle the highly unstable flames in which the less extensive stable regime makes it extremely challenging when extrapolating stretch-free flame speed.

$$F = \left( \frac{Pe}{Pe_{cl}} \frac{n_{lcl}}{n_l} \right)^{1/3} \quad (11)$$

where  $Pe$  is Peclet number ( $r_u/\delta$ ),  $n_l$  is the smallest unstable wave-number, associated with the largest unstable wavelength,  $n_{lcl}$  is  $n_l$  at the critical flame radius. Values of  $n_{lcl}$  and  $n_l$  could be estimated from the theory of [2].

Then the theoretical modified flame speed without instabilities is calculated as:

$$S = S_n/F \quad (12)$$

The linear extrapolation of raw  $S_n$  and the derived values of  $S$  against  $\alpha$  was then employed to obtain the stretch-free value of flame speed and hence  $u_l$ .

All the above parameters in Eqs. (1) to (12) can be obtained by Schlieren ciné-photography and GASEQ code [33].

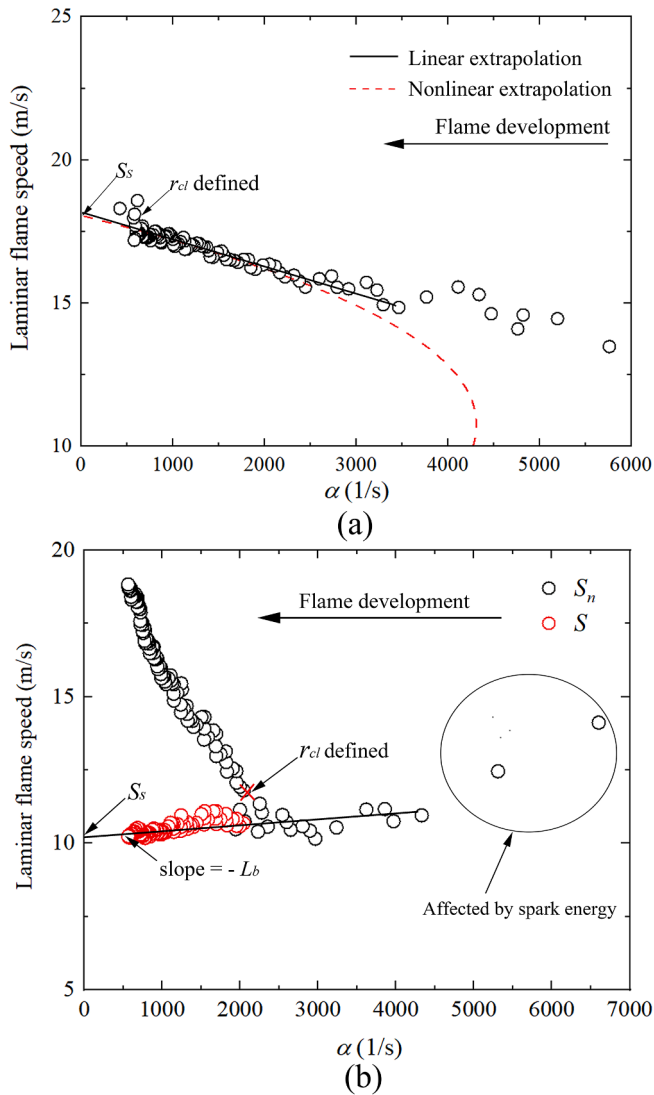


**Fig. 5.** Laminar flame speed at different flame stretch rate for hydrogen/air mixtures. (a) solid black line (Eq. (2)) and dashed red line (Eq. (4)) denote linear and nonlinear relationships at  $\phi = 2.0$ ,  $T_i = 300$  K,  $P_i = 0.1$  MPa, (b) black circles ( $S_n$ ) and red circles ( $S$ ) denote experimental and theoretical flame speed at  $\phi = 0.8$ ,  $T_i = 300$  K,  $P_i = 0.3$  MPa. (For interpretation of the references to colour in this figure legend, the reader is referred to the web version of this article.)

## 4. Results and discussions

### 4.1. Flame topography

In the present study, the onset of cellularity and instability of expanding spherical flames have been evaluated experimentally. The effect of  $P_i$  on expanding hydrogen-air flames is presented in Fig. 2 at fixed  $T_i = 360$  K and  $\phi = 0.8$ . Flame morphology shows that the hydrogen/air flames feature a noticeable cellular structure, especially under  $P_i$  equals 0.3 and 0.5 MPa. Compared with hydrocarbons [20–24] which have a relatively late onset of cellularity, hydrogen flame surface presents a developing cellular structure at the early stage of propagation. Fig. 2 also shows that increasing  $P_i$  results in the earlier occurrence of cellular instability and more obvious wrinkles. The enhancement of cellular instability with elevated  $P_i$  was due to the increasing sensitivity to hydrodynamic disturbances with the decreasing flame thickness, and the increase of flame response to the unstable thermal diffusion effects.

The effect of  $T_i$  on expanding hydrogen-air flames is presented in Fig. 3 at fixed  $P_i = 0.1$  MPa and  $\phi = 0.8$ . With an increase of  $T_i$ , the destabilizing propensity of the hydrogen-air flames is slightly reduced albeit many cracks still exist on the flame surface. Some cracks on the flame front would disappear with the increase of  $T_i$ , and the flame front almost keeps smooth during the propagation within the most view field of windows, namely the cellular instability has not appeared yet until  $R_{sch}$  equals approximately 60 mm.

The effect of mixture strength on expanding hydrogen-air flames is presented in Fig. 4 at the initial condition of 360 K and 0.1 MPa. Fig. 4 shows that intense cellularity occurs early in a flame at  $\phi = 0.4$ , but the onset of cells occurs at larger radii with increasing  $\phi$  until at  $\phi = 1.0$ , only weak cellularity is shown even at the largest measured radius of 60 mm. For hydrogen/air flames, the decline in cellular instability should be attributed mainly to the increase of the thermal diffusion instability. Though the flame temperature determined by mixture strength plays a role on cellular instability, the quantitative study on this effect is out of the scope of this work. The above observation shows that the flame becomes cellular at a given radius, which results in a rapid increase in flame speed. More details about defining the onset of instability, using the current experimental setup, can be found in [20,29]. Additionally, stretch is the means of stability. Therefore, the measured flame speed is plotted against the flame stretch rate in Fig. 5. Immediately after ignition, the stretch rate is strong enough to smooth any disturbances on the flame surface. However, as the flame grows, the stretch rate progressively decreases. The rapid increase in the flame speed after the critical stretch rate corresponding to the onset of cellularity shows a transition into cellular flame propagation. At small radii the flame is affected by the spark. Hence, a decision must be made about when the spark effect becomes negligible. At the other end of large radii and small stretches, flames become unstable and cellular which can cause the flame to

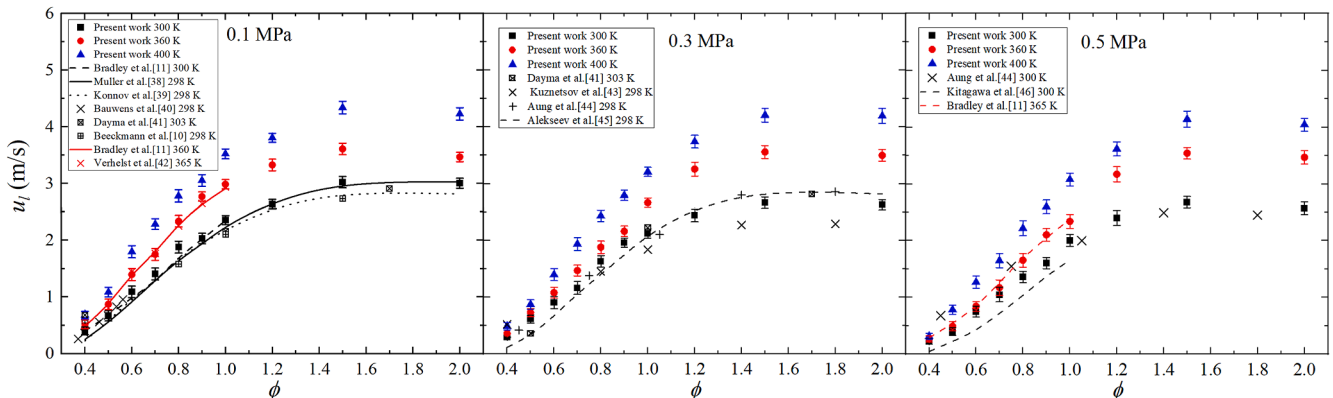


**Fig. 6.** Laminar burning velocities of hydrogen-air flames at  $\phi = 0.4$ – $2.0$ ,  $T_i = 300, 360, 400$  K,  $P_i = 0.1, 0.3, 0.5$  MPa. Error bands are for experiments.

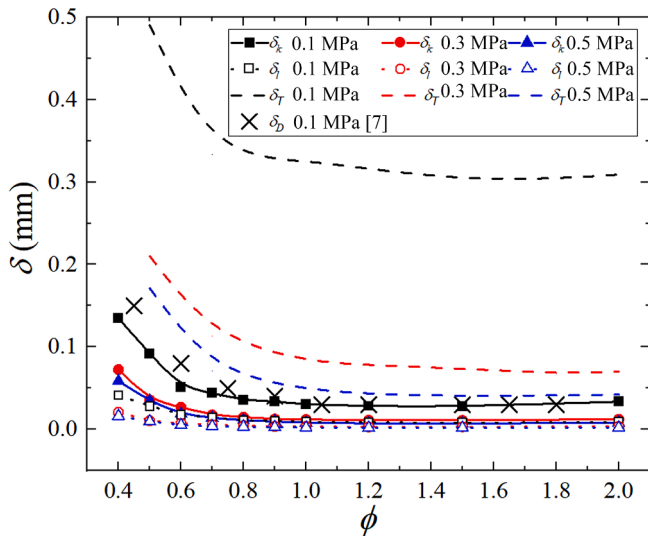


Fig. 7. Laminar flame thickness against  $\delta_D$  at  $300 \pm 2$  K,  $\delta_i$  is calculated by Eq. (5),  $\delta_T$  is calculated by Eq. (6),  $\delta_k$  is calculated by Eq. (7),  $\delta_D$  is extracted from [7].

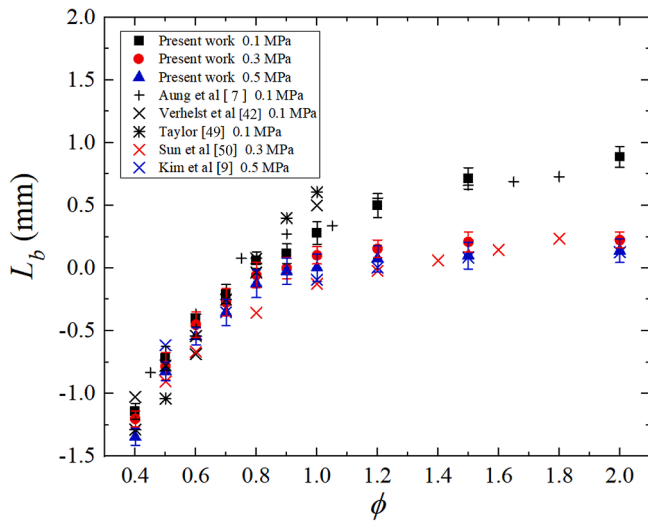


Fig. 8. Experimental values of  $L_b$  against  $\phi$  at  $P_i = 0.1, 0.3,$  and  $0.5$  MPa,  $T_i = 300$  K. Error bands are for experiments.

accelerate due to a cellular increase in surface area.

There are several possible sources of uncertainty in measuring laminar burning velocity and critical Karlovitz number. These sources have been discussed in detail, in [31], using the current experimental setup. It has been concluded that the choice of flame radius range for extrapolation and extrapolation type are important sources that can cause a high uncertainty in laminar burning velocity and Karlovitz number. The source of uncertainty can be negligible if a suitable range of extrapolation ( $r_{cl} > r_u > 10$  mm) is used as well as a suitable type of extrapolation (i.e. linear and nonlinear). Unstretched flame speeds have been derived by various linear and nonlinear extrapolations [11,30,31,34-36]. The comparison between the linear method (Eq. (2)) and the nonlinear method (Eq. (4)) is shown in Fig. 5(a) and suggests no obvious effect of the extrapolation discrepancy on  $S_s$ . In order to investigate the stretch effect ( $L$  and  $Ma$ ) on the flame instability, the classic and widely used linear model based on the stretch was adopted in this study. Furthermore, in order to compensate for the uncertainty of unstretched flame speed caused by the narrow stability region at high pressure (only a few points, see Fig. 5(b)), Eqs. (11 and 12) can calculate

the modified flame speed without instabilities at low stretch rate region,  $S$ , for extrapolation. Then the valid region for the determination of Markstein lengths lies between these points. A linear curve fit is then extrapolated back to zero stretch to yield the unstretched flame speed and the Markstein length, given by the negative of the gradient of the linear extrapolation.

## 4.2. Flame characteristics

### 4.2.1. Burning velocity and flame thickness

It is essential and informative to present the unstretched laminar burning velocity,  $u_l$  over different conditions derived from Eq. (3), which is shown in Fig. 6. For clarity, comparisons with previous data [10,11,37-45] are presented. The present results, at atmospheric  $T_i$ , are in good agreement with the literature. However, very few experimental data are reported for hydrogen at high  $T_i$  ( $\geq 400$  K). Consequently, this study fills the data gap of hydrogen laminar burning velocity at high-temperature ranges.

The GRI 3.0 combustion kinetics [46] was used to study the flame propagation of hydrogen-air mixtures using 1D premixed flame code implemented in the Chemkin-Pro 19.1 software [47]. The predicted temperature profile was then used to derive the hydrogen flame thickness  $\delta_T$  following the temperature gradient method (Eq. (6)).  $\delta_i$  and  $\delta_k$  derived from Eqs. (5 and 7) respectively are presented in Fig. 7 as well. In addition, another expression of flame thickness  $\delta_D$  as the ratio of the mass diffusivity of the fuel in unburned gas over the laminar burning velocity [7] is presented herein for comparison and verification. It shows  $\delta_D$  and  $\delta_k$  have good agreement, but both are more than twice higher than  $\delta_i$  and less than  $\delta_T$ .  $H$  atoms move quickly to the leading edge, where they start reacting more quickly than in hydrocarbon flames, reducing the preheat zone [32]. Hence,  $\delta_k$  is adopted for the hydrogen-air mixtures in the present work.

### 4.2.2. Markstein length and number

The burned gas Markstein lengths  $L_b$  are determined using a linear curve fitting method as described in Section 4.1. Markstein length keeps almost constant at conditions with various initial temperatures. Fig. 8 shows the variation of  $L_b$  with respect to  $\phi$  at  $T_i = 300$  K and various  $P_i$  values.  $L_b$  reported in [7,9,41,48,49] are also shown in Fig. 8 for the purpose of comparison. The literature and the present work show a good agreement.

Based on the fact that the present flame thickness and Markstein lengths are consistent with the literature. Therefore, it is asserted that the value of Markstein number  $Ma_b$  expressed as  $L_b$  normalised by  $\delta_k$ , is reasonable and accurate in the scope of this work. The results are given in Fig. 9 for  $\phi$  up to 2.0 at different  $P_i$  and  $T_i$ . For  $\phi > 0.7$  at high pressures (i.e. 0.3 and 0.5 MPa), the uncertainty became noticeable. At 0.1 MPa, values of  $Ma_b$  became positive at  $\phi > 0.8$ . Similarly, at 0.3 and 0.5 MPa, the presented values of  $Ma_b$  were negative in the lean mixture, and then gradually become positive as  $\phi$  increases. Markstein number can characterize the effect of stretching on flame stability, and is related to the beginning of cell instability.

### 4.2.3. Critical dimensionless numbers

$Pe_{cl}$  is an important parameter for practical applications. Many researchers related the  $Pe_{cl}$  with  $Ma_{sr}$  directly [20-23]. Strain effect on burned side of the flame surface accounts for the dominant hydrodynamic instability. However, curvature stretch exists during the whole expansion of flame in the laminar regime. Therefore, the overall burned gas Markstein number  $Ma_b$  accounting for the contributions of both strain rate and flame curvature is adopted to correlate with the  $Pe_{cl}$ . Experimental values of  $r_{cl}$  and  $Pe_{cl}$  against  $\phi$  at different  $P_i$  and  $T_i$  are shown in Figs. 10 and 11, respectively. Coupled with Figs. 2 and 3, it is clearly showing that the onset of instabilities occurs at values of  $r_{cl}$  and  $Pe_{cl}$  that decrease as the  $P_i$  increases. For hydrogen-air flames,  $r_{cl}$  and  $Pe_{cl}$  increase as  $\phi$  increases, indicating a more stable flame. This is obvious in

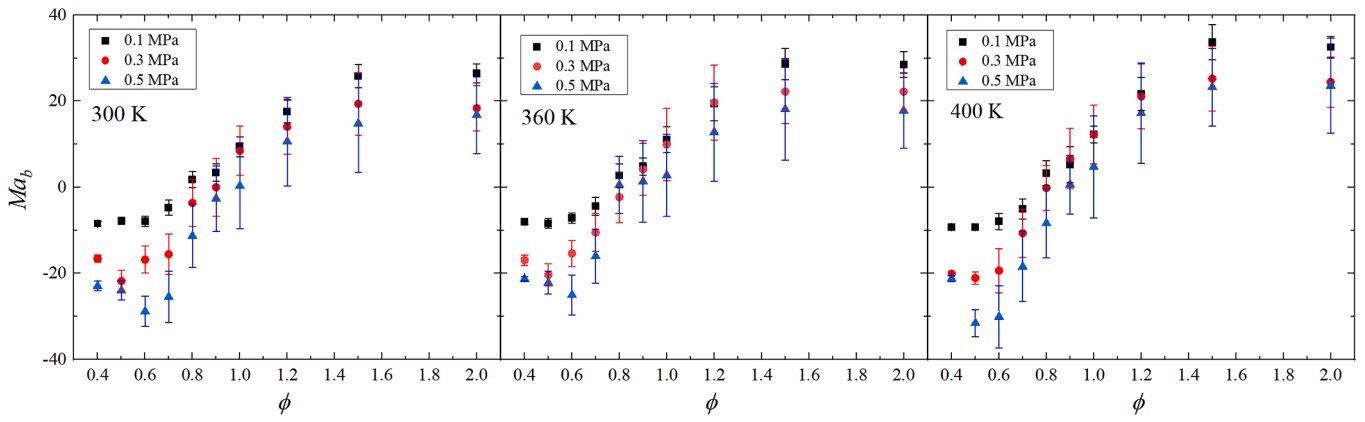


Fig. 9. Experimental values of  $Ma_b$  against  $\phi$  at  $P_i = 0.1, 0.3,$  and  $0.5$  MPa,  $T_i = 300, 360$  and  $400$  K. Error bands are for experiments.

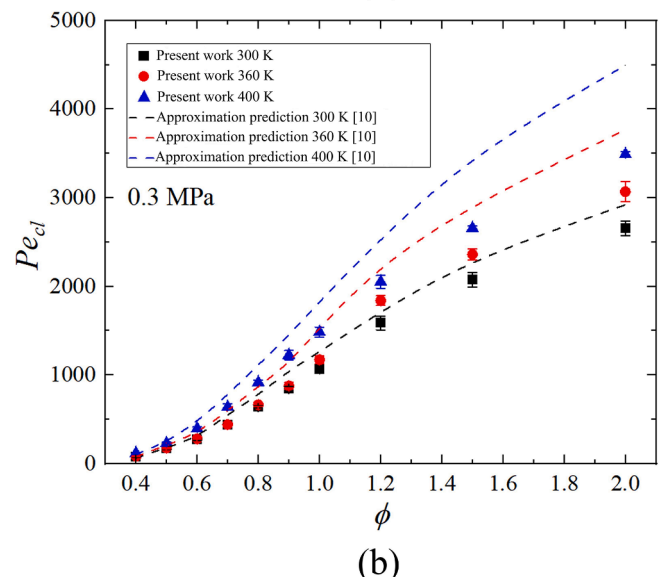
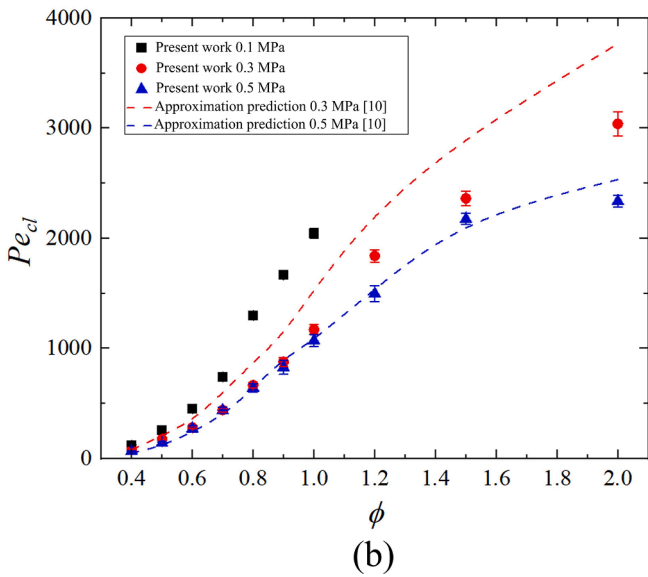
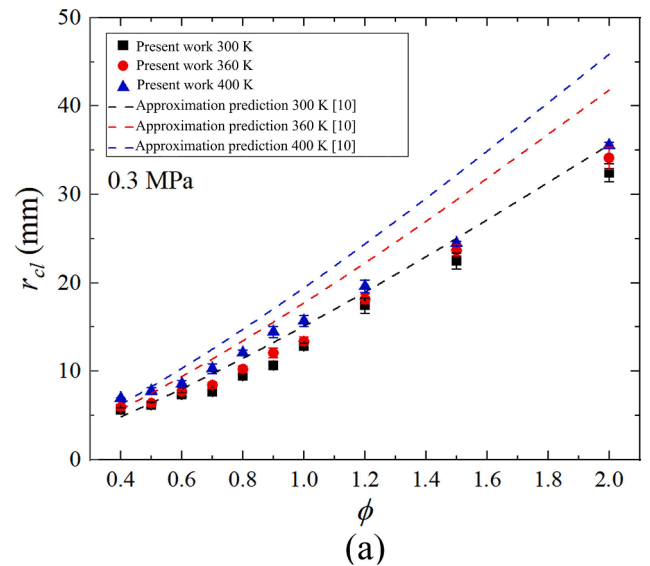
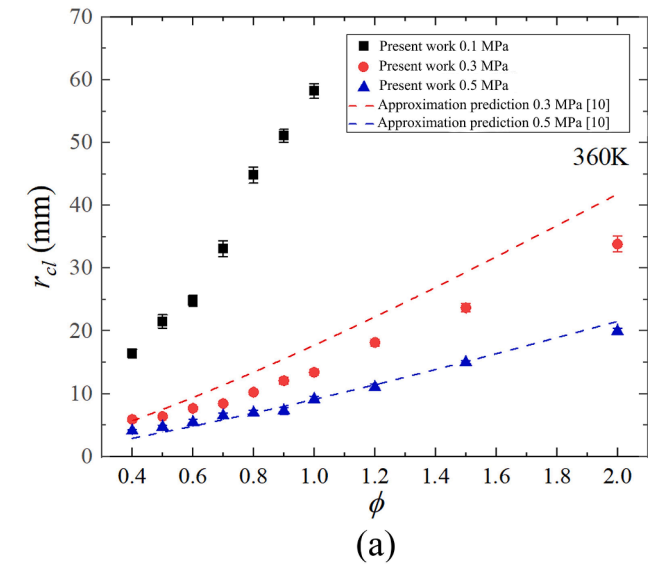


Fig. 10. Experimental values of critical points against  $\phi$  at  $P_i = 0.1, 0.3,$  and  $0.5$  MPa,  $T_i = 360$  K. (a)  $r_{cl}$ , (b)  $Pe_{cl}$ . Error bands are for experiments.

Fig. 11. Experimental values of critical points against  $\phi$  at  $T_i = 300, 360,$  and  $400$  K,  $P_i = 0.3$  MPa. (a)  $r_{cl}$ , (b)  $Pe_{cl}$ . Error bands are for experiments.

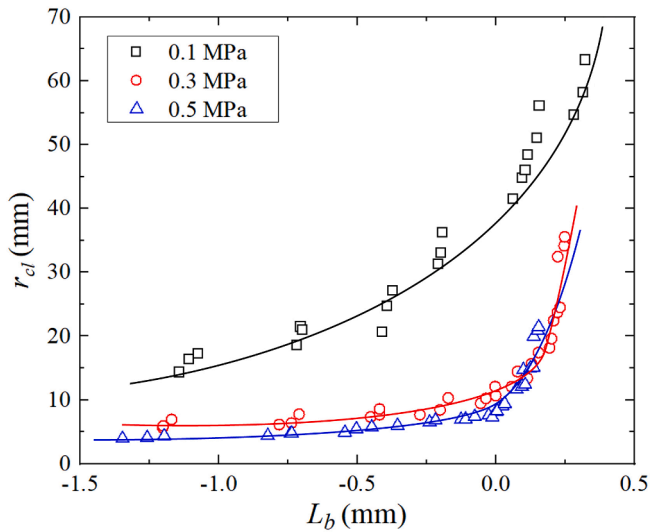


Fig. 12. Variations of  $r_{cl}$  with respect to  $L_b$  covering  $P_i = 0.1, 0.3, 0.5$  MPa and  $T_i = 300, 360, 400$  K. Solid lines are the fitting curves.

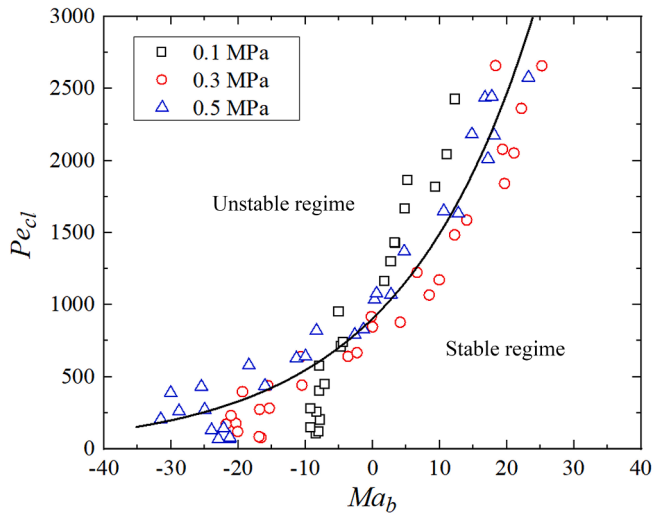


Fig. 13. Variations of  $Pe_{cl}$  with respect to  $Ma_b$  covering  $T_i = 300, 360, 400$  K and  $P_i = 0.1, 0.3, 0.5$  MPa. One straight solid line is derived from the present data points, which splits the  $Pe_{cl}$ - $Ma_b$  diagram into two parts representing unstable- and stable- regimes.

Fig. 10 at 0.1 MPa. On the contrary, the increase of  $T_i$  delays the onset of flame instability slightly. The reduced  $Pe_{cl}$  and flame thickness slightly destabilize the flame surface as  $T_i$  increases. Critical radius,  $r_{cl}$  and  $Pe_{cl}$  ( $r_{cl}/\delta_k$ ) using approximation formula [10] are calculated and plotted in Fig. 10 and Fig. 11. Those results are in a good agreement with the current results, with a slight difference observed on the rich side.

### 4.3. Identification of stable regime

Critical flame radius,  $r_{cl}$  can be easily and directly observed by Schlieren ciné-photography, and the dependency of  $r_{cl}$  on  $L_b$  with their correlations are presented in Fig. 12. The aforementioned sections demonstrate that variations of  $T_i$  from 300 to 400 K do not influence the distributions of critical points much, revealing that flame instability has little dependence on  $T_i$  within the given range. As it can be seen that  $r_{cl}$  increases the increase with  $L_b$ , which seems is an exponential correlation for  $r_{cl}$  ( $L_b$ ).

Table 1  
Correlations of critical numbers and Markstein numbers.

Author	Fuel	Critical number	Markstein number	Correlation
Bradley et al [20]	iso-octane/air	$Pe_{cl}$	$Ma_{sr}$	$Pe_{cl} = 188Ma_{sr} + 2320$
Bradley et al [21]	methane/air	$Pe_{cl}$	$Ma_{sr}$	$Pe_{cl} = 177Ma_{sr} + 2177$
Gu et al [22]	ethanol/air	$Pe_{cl}$	$Ma_{sr}$	$Pe_{cl} = 1808.6exp(0.103Ma_{sr})$
Mannaa et al [23]	gasoline fuels	$Pe_{cl}$	$Ma_{sr}$	$Pe_{cl} = 1230.4exp(0.31Ma_{sr})$
Kim et al [9]	propane/air	$Pe_{cl}$	$Ma_b$	$Pe_{cl} = 438Ma_b + 2500$
Kim et al [24]	hydrogen/air	$Pe_{cl}$	$Ma_b$	$Pe_{cl} = 69Ma_b + 1595$
Oppong et al [50]	ethyl acetate	$Pe_{cl}$	$Ma_b$	$Pe_{cl} = 52.31Ma_b + 260.4$
This study	hydrogen/air	$Pe_{cl}$	$Ma_b$	$Pe_{cl} = 900exp(0.05Ma_b)$
Bradley et al [20]	iso-octane/air	$K_{cl}$	$Ma_{sr}$	$K_{cl} = 0.0075exp(-0.123Ma_{sr})$
Mannaa et al [23]	gasoline fuels	$K_{cl}$	$Ma_b$	$K_{cl} = 0.012exp(-0.058Ma_b)$
Kim et al [24]	hydrogen/air	$K_{cl}$	$Ma_{sr}$	$K_{cl} = 0.01554exp(-0.195Ma_{sr})$
Bradley et al [26]	nine fuels	$K_{cl}$	$Ma_{sr}$	$K_{cl} = 0.0128exp(-0.32Ma_{sr})$

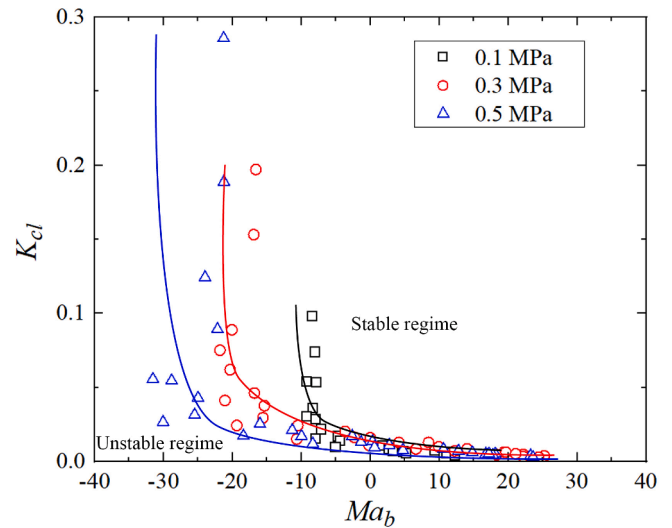


Fig. 14. Values of  $K_{cl}$  with respect to  $Ma_b$  at  $P_i = 0.1, 0.3, 0.5$  MPa. Solid lines are the curve fittings of the present data points of 0.1, 0.3, 0.5 MPa, which splits the  $K_{cl}$ - $Ma_b$  diagram into two parts representing unstable- and stable- regimes respectively.

In order to find the generality of flame instability regime,  $r_{cl}$  and  $L_b$  are dimensionless into  $Pe_{cl}$  and  $Ma_b$  to find the generality of hydrogen/air mixture at a wide range of initial conditions. Fig. 13 shows the variation of  $Pe_{cl}$  with respect to  $Ma_b$  at  $T_i = 300, 360$  and  $400$  K. Values of  $Pe_{cl}$  decreased with a decrease in  $Ma_b$ . Therefore, the propensity of the early smooth flame to cellularity increases as  $Ma_b$  decreases, and the stable regime is significantly reduced especially for highly negative  $Ma_b$ . The inherent hydrodynamic instability may be suppressed by stretch with positive  $Ma_b$ . Since the data points scatter appear to be distributed nonlinearly, an exponential fitting equation of  $Pe_{cl}$ - $Ma_b$  (Eq. (13)) was developed and presented in Fig. 13:

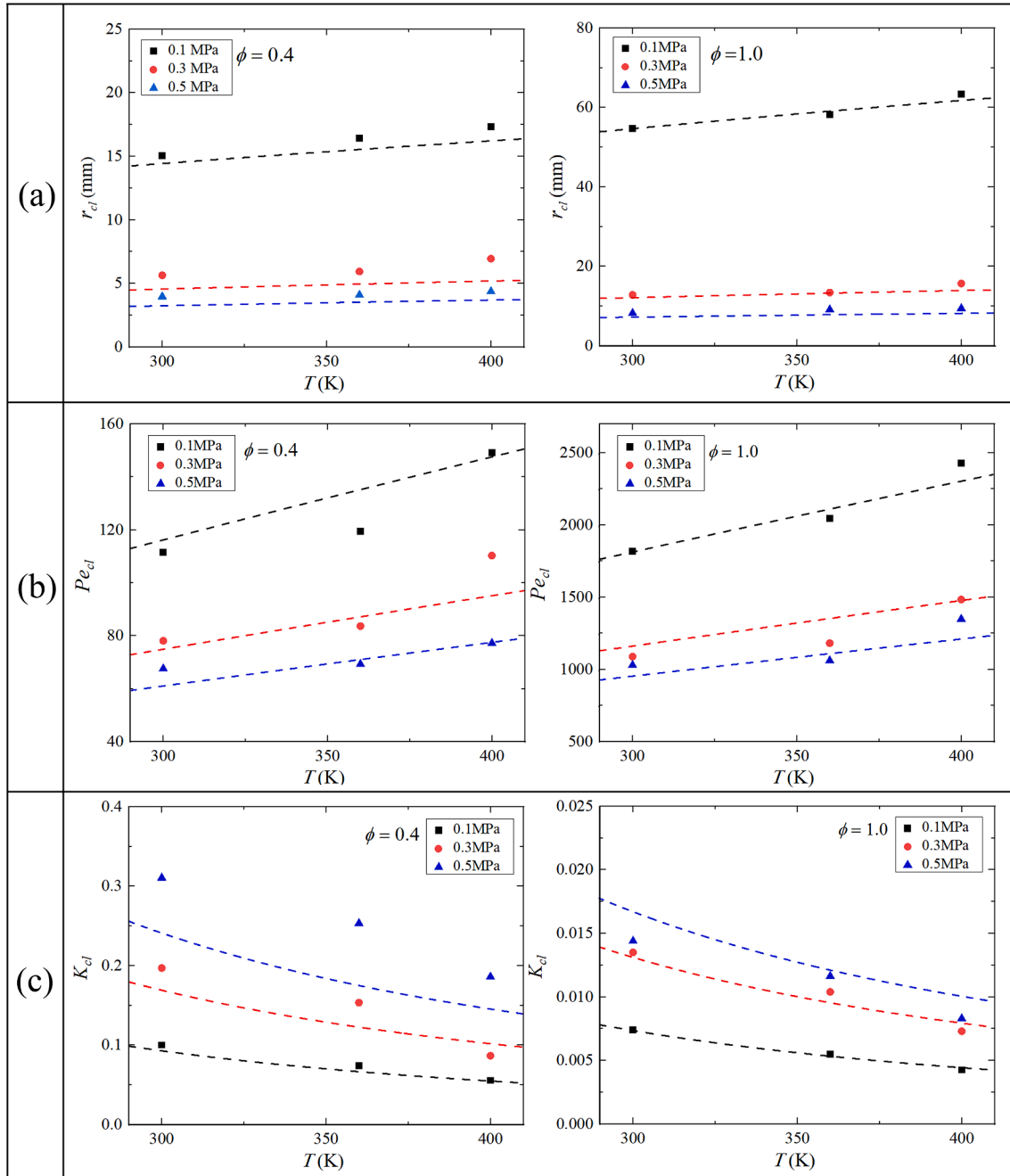


Fig. 15. Critical parameters of hydrogen/air flames against different  $T_i$  at  $P_i = 0.1, 0.3, 0.5$  MPa and  $\phi = 0.4$  and  $1.0$ . (a)  $r_{cd}$ , (b)  $Pe_{cb}$ , (c)  $K_{cb}$ . The dashed lines represent the approximated results using Eqs. (17)–(19). Fitting lines of different colours correspond to different pressure test data points.

$$Pe_{cl} = 900exp(0.05Ma_b), R^2 = 0.9 \quad (13)$$

The closer the  $R^2$  value is to 1, the higher the coincidence degree is, and the closer it is to 0, the lower the coincidence degree is.

Fig. 13 takes into account both low pressure (0.1 MPa) and high pressure (0.3&0.5 MPa) impact on the stability property of hydrogen flames. Despite the low-pressure data slightly offset from correlation, the combination of non-dimensional parameters,  $Pe_{cl}$  and  $Ma_b$ , are reasonably identifying the boundary between the stable regime and unstable regime.

Previous correlations [9,20-24,50] between  $Pe_{cl}$  and Markstein numbers ( $Ma_{sr}$ ,  $Ma_b$ ) of different mixtures are concluded in Table 1. Although these expressions showed a considerable quantitative disagreement, a similar increasing tendency of  $Pe_{cl}$  with respect to  $Ma_b$  has been identified for all conditions, including this study. Critical laminar Karlovitz number,  $K_{cl}$ , can be considered to be a more relevant parameter evaluating flame instability than  $Pe_{cl}$ , described in section 3. In previous studies, the expressions [20,23,24,26] of  $K_{cl}$  with Markstein numbers ( $Ma_{sr}$ ,  $Ma_b$ ) are reported in Table 1

as well. Due to the different characteristics from other gases mentioned before, hydrogen requires to be studied separately in particular. Variations of  $K_{cl}$  with  $Ma_b$  at 0.1, 0.3, 0.5 MPa are presented in Fig. 14.  $K_{cl}$  increases with the decrease of  $Ma_b$ , which is paralleled by a similar phenomenon in mildly turbulent flames [11].

The accuracy of the dependency of  $r_{cl}$ ,  $K_{cl}$  on  $Pe_{cl}$  on  $Ma_b$  is discussed below. The flame morphology develops a full cellular structure straightforward after its initiation at elevated  $P_i$ , which brings some uncertainties in data analysis and formula fitting. Such flame instabilities throw into question the utility of  $u_l$  and  $L_b$  for high pressure, very unstable, flames. The theoretic modified flame speed  $S$  without instability could provide a potential solution. Note the uncertainty associated with estimating  $Ma_b$  increases when  $Ma_b$  gets a large negative value, which usually happens at high pressure and high equivalence ratios. Comparison with theoretical  $Ma_b$  value would be useful. It also must be clarified that the  $Pe_{cl}$  and  $K_{cl}$  obtained in this study are different from the previous values for different hydrogen flame thickness calculation methods. The previous approximate calculation formula  $\delta_l \cong \nu/u_l$  or the temperature gradient method is inappropriate for hydrogen, which has a great impact on the quantification and analysis of  $Pe_{cl}$  and  $K_{cl}$ .

Note that the dependency of  $Pe_{cl}$  and  $K_{cl}$  on the  $Ma_b$  can be found and the related correlations using these dimensionless groups can be established. From a practical point of view, although  $Pe_{cl}$  and  $K_{cl}$  are dependent on  $Ma_b$ , for hydrogen, the inaccurate  $Ma_b$  under high pressure reduces its reliability. Even if very accurate formulas are established to predict  $Pe_{cl}$  and  $K_{cl}$  based on  $Ma_b$ , much effort and time are essential to get  $Ma_b$  by experiments, while  $Pe_{cl}$  and  $K_{cl}$  are the relatively easy and accurate parameters to obtain. In order to predict the onset of instability in laminar hydrogen flames effectively and concisely, quantified by  $r_{cl}$ ,  $Pe_{cl}$ ,  $K_{cl}$ , new prediction models are required to be proposed.

#### 4.4. Prediction of flame instability

As shown in Fig. 2 and Fig. 3, Fig. 10 and Fig. 11 and Eq. (13), in all cases, increasing the temperature and equivalence ratio, decreasing the pressure causes the increase in  $r_{cl}$ ,  $Pe_{cl}$ , the decrease in  $K_{cl}$ . It is sensible to establish the empirical expressions for the experimentally obtained critical parameters ( $r_{cl}$ ,  $Pe_{cl}$ ,  $K_{cl}$ ) as a function of pressure, temperature and equivalence ratio:

$$\frac{r_{cl}}{r_{cl,0}} = \left(\frac{T_i}{T_0}\right)^{\alpha_r} \left(\frac{P_i}{P_0}\right)^{\beta_r} \left(\frac{\phi}{\phi_0}\right)^{\gamma_r} \quad (14)$$

$$\frac{Pe_{cl}}{Pe_{cl,0}} = \left(\frac{T_i}{T_0}\right)^{\alpha_p} \left(\frac{P_i}{P_0}\right)^{\beta_p} \left(\frac{\phi}{\phi_0}\right)^{\gamma_p} \quad (15)$$

$$\frac{K_{cl}}{K_{cl,0}} = \left(\frac{T_i}{T_0}\right)^{\alpha_k} \left(\frac{P_i}{P_0}\right)^{\beta_k} \left(\frac{\phi}{\phi_0}\right)^{\gamma_k} \quad (16)$$

Here, the critical radius  $r_{cl,0}$  (55 mm),  $Pe_{cl,0}$  (1817) and  $K_{cl,0}$  (0.0074) from the present data set are chosen as normalisation parameters at  $T_0 = 300$  K,  $P_0 = 0.1$  MPa and  $\phi_0 = 1.0$ . The temperature coefficients ( $\alpha_r$ ,  $\alpha_p$ ,  $\alpha_k$ ), pressure coefficients ( $\beta_r$ ,  $\beta_p$ ,  $\beta_k$ ) and equivalence ratio coefficients ( $\gamma_r$ ,  $\gamma_p$ ,  $\gamma_k$ ) are obtained over the range of 300–400 K, 0.1–0.5 MPa, and equivalence ratios from 0.4 to 2.0. The least-square fitting is used to combine all available data points for each estimate and arrive at the following conclusion:

$$\frac{r_{cl}}{r_{cl,0}} = \left(\frac{T_i}{T_0}\right)^{0.45} \left(\frac{P_i}{P_0}\right)^{-1.1} \left(\frac{\phi}{\phi_0}\right)^{1.4} \quad (17)$$

$$\frac{Pe_{cl}}{Pe_{cl,0}} = \left(\frac{T_i}{T_0}\right)^{0.83} \left(\frac{P_i}{P_0}\right)^{-0.4} \left(\frac{\phi}{\phi_0}\right)^3 \quad (18)$$

$$\frac{K_{cl}}{K_{cl,0}} = \left(\frac{T_i}{T_0}\right)^{-1.75} \left(\frac{P_i}{P_0}\right)^{0.52} \left(\frac{\phi}{\phi_0}\right)^{-2.8} \quad (19)$$

Due to the finite size of the Leeds MK-II (a 380 mm diameter vessel) and optical access (150 mm diameter quartz windows), the critical radius at rich hydrogen-air mixtures under atmospheric conditions cannot be observed. Example values of approximated  $r_{cl}$ ,  $Pe_{cl}$  and  $K_{cl}$  using Eqs. (17) to (19) are presented and compared with measured data in Fig. 15. The fitting equations perform well in predicting  $r_{cl}$ ,  $Pe_{cl}$  and  $K_{cl}$  that reflect the onset of flame instability except for a slight deviation for the lean mixture ( $\phi = 0.4$ ) at the high-pressure condition ( $P_i = 0.5$  MPa).

The cellular unstable laminar flame has fundamental and practical significance by dint of its intrinsic acceleration without any external sources, as demonstrated previously for the spherically expanding flame [12]. Flame instability shows different forms and scales. These instabilities may be harmful and detrimental when they occur in actual systems. For example, they can cause conditions that may cause damage and mechanical failure to the combustion device. However, in other cases, they may help to enhance mixing and increase combustion rate. As stated in [51], the enhancement at the flame surface is a combination of the combustion-induced turbulence and the wrinkling by the thermal diffusion instability. Therefore, an in-depth understanding of hydrogen combustion characteristics is necessary and essential for further scientific applications, especially for gas turbines fueled by hydrogen-air mixtures.

This cellularity phenomenon is very important in all practical contexts. The increase of  $P_i$  combined with the decrease in Markstein number enhances instabilities. Further work is required to get a better understanding of these practical effects. These generalized findings from small-scale laboratory flame explosions provide a novel method for predicting  $r_{cl}$ ,  $Pe_{cl}$  and  $K_{cl}$  under a wide range of temperatures and pressures. Since the critical parameters reflect the flame instability, the approximated values could be used to assess the severity of large-scale atmospheric explosions once the thermal diffusion instability is identified to be responsible for deflagration to detonation transition in expanding flame. In addition to the obvious practical relevance of the work to the hazards of large-scale flame explosions, the observed structural changes and instabilities are also related to laminar flamelet modelling of turbulent combustion, especially at high pressure.

### 5. Conclusions

1. This work provides a data set for the further development and verification of hydrogen flame laminar burning velocity and instability models, including  $u_l$ ,  $Ma_b$  and  $r_{cl}$ ,  $Pe_{cl}$ ,  $K_{cl}$ .
2.  $P_i$  has a significant effect on the flame stability, compared with those of equivalence ratio and  $T_i$ . Although the pressure change hardly affects Lewis number and the density ratio of unburned gas to burned gas, which means that it does not enhance uneven thermal diffusion instability, it affects the flame more directly by changing the flame thickness. The increase of  $P_i$  significantly weakens the flame front and makes it more prone to instability. Higher  $P_i$  also leads to more cells with smaller average sizes.
3. It is difficult to theoretically or experimentally obtain hydrogen flame thickness. Previous simple calculations for the flame thickness of preheat zone are not applicable for hydrogen and their use results in many contradictions. For critical radius, figures and formulas can reasonably express and predict its monotonous change. However, for  $Pe_{cl}(r_{cl}/\delta_k)$ , it is also largely satisfied that the increment of temperature leads to the increase of its value, but from the perspective of pressure, when  $P_i$  increases from 0.3 MPa to 0.5 MPa, much reduced preheat zone of hydrogen due to the increase of pressure results in the increase of  $Pe_{cl}$ .
4. The great dependence of  $r_{cl}$ ,  $Pe_{cl}$  and  $K_{cl}$  on  $Ma_b$  can be found and the expressions for the  $r_{cl}$ ,  $Pe_{cl}$  and  $K_{cl}$  on  $Ma_b$  are explored, most of them are in good agreement with experimental values.
5. Novel empirical correlations and expressions for predicting the onset of flame instability are also proposed in this study, which are in good

agreement with the experimental values. This dimensionless group-based correlation provides alternative means for predicting large atmospheric flame explosions via lab-scale but high-pressure experiments.

### Declaration of Competing Interest

The authors declare that they have no known competing financial interests or personal relationships that could have appeared to influence the work reported in this paper.

### Data availability

Data will be made available on request.

### Acknowledgments

The authors thank EPSRC (Grant No. EP/W002299/1) for the financial support. Yu Xie acknowledges the China Scholarship Council and University of Leeds for a joint PhD scholarship (CSC202008350141). Authors would like to acknowledge the valuable discussions with Dr. Malcolm Lawes and Pro. Derek Bradley.

### Appendix A

Tables A1-A3.

**Table A1**  
Experimental data at 300 K.

	$\phi$	$\rho_u/\rho_b$	$Ss$ (m/s)	$u_l$ ( m/s)	$\delta_k$ (mm)	$L_b$ (mm)	$Ma_b$	$r_{cl}$ (mm)	$Pe_{cl}$	$K_{cl}$
0.1 MPa	0.4	4.420	1.95	0.44	0.1347	-1.142	-8.48	14.40	106.85	0.1000
	0.5	5.012	3.34	0.67	0.0918	-0.719	-7.84	18.62	202.87	0.0548
	0.6	5.532	6.03	1.09	0.0515	-0.410	-7.96	20.69	401.61	0.0288
	0.7	5.981	8.41	1.41	0.0441	-0.209	-4.74	31.33	710.80	0.0170
	0.8	6.361	11.95	1.88	0.0357	0.063	1.76	41.55	1164.22	0.0109
	0.9	6.666	13.53	2.03	0.0340	0.115	3.38	48.47	1426.56	0.0092
	1	6.863	16.15	2.35	0.0301	0.281	9.34	54.72	1817.44	0.0074
	1.2	6.82495	17.99	2.64	0.0283	0.498	17.59	-	-	-
	1.5	6.54233	18.93	2.89	0.0277	0.716	25.84	-	-	-
	2	6.04564	18.16	2.66	0.0336	0.887	26.45	-	-	-
0.3 MPa	0.4	4.418	1.30	0.29	0.0724	-1.202	-16.60	5.65	78.05	0.1970
	0.5	5.013	3.08	0.61	0.0358	-0.781	-21.81	6.15	171.59	0.0751
	0.6	5.535	5.00	0.90	0.0268	-0.451	-16.81	7.34	273.40	0.0482
	0.7	5.992	6.96	1.16	0.0175	-0.273	-15.58	7.70	438.49	0.0317
	0.8	6.385	10.21	1.63	0.0148	-0.054	-3.66	9.48	640.93	0.0212
	0.9	6.712	13.16	1.96	0.0126	0.000	0.00	10.69	845.87	0.0166
	1	6.937	14.70	2.12	0.0120	0.102	8.45	12.81	1066.82	0.0135
	1.2	6.864	16.74	2.44	0.0110	0.154	14.05	17.44	1586.87	0.0087
	1.5	6.562	17.48	2.66	0.0108	0.209	19.38	22.47	2078.11	0.0062
	2	6.100	16.03	2.63	0.0122	0.224	18.35	32.45	2658.73	0.0045
0.5 MPa	0.4	4.418	1.00	0.23	0.0587	-1.347	-22.95	3.97	67.55	0.3105
	0.5	5.013	2.01	0.40	0.0343	-0.823	-23.98	4.41	128.65	0.1393
	0.6	5.535	4.15	0.75	0.0189	-0.544	-28.83	4.92	260.61	0.0630
	0.7	5.992	6.29	1.05	0.0139	-0.354	-25.49	6.00	431.85	0.0371
	0.8	6.385	8.69	1.36	0.0110	-0.125	-11.32	6.94	628.55	0.0246
	0.9	6.712	10.77	1.60	0.0096	-0.025	-2.64	7.62	791.68	0.0192
	1	6.937	13.89	2.00	0.0079	0.003	0.31	8.21	1034.57	0.0144
	1.2	6.878	16.50	2.40	0.0071	0.075	10.61	11.65	1648.48	0.0086
	1.5	6.569	17.60	2.68	0.0068	0.100	14.81	14.73	2182.01	0.0061
	2	6.103	15.68	2.57	0.0082	0.137	16.76	19.97	2436.62	0.0051

**Table A2**  
Experimental data at 360 K.

	$\phi$	$\rho_u/\rho_b$	$Ss$ (m/s)	$u_l$ ( m/s)	$\delta_k$ (mm)	$L_b$ (mm)	$Ma_b$	$r_{cl}$ (mm)	$Pe_{cl}$	$K_{cl}$
0.1 MPa	0.4	3.814	1.97	0.52	0.1375	-1.109	-8.06	16.41	119.37	0.0739
	0.5	4.304	3.75	0.87	0.0844	-0.705	-8.35	21.53	254.93	0.0371
	0.6	4.730	6.60	1.40	0.0551	-0.393	-7.13	24.81	449.84	0.0220
	0.7	5.097	8.92	1.75	0.0447	-0.198	-4.44	33.11	741.19	0.0139
	0.8	5.404	12.62	2.34	0.0345	0.094	2.73	44.82	1300.54	0.0083
	0.9	5.646	15.64	2.77	0.0306	0.148	4.82	51.09	1667.13	0.0066
	1	5.800	17.33	2.99	0.0285	0.314	11.03	58.22	2044.95	0.0055
	1.2	5.508	18.32	3.33	0.0270	0.523	19.39	/	/	/
	1.5	5.558	20.06	3.61	0.0274	0.784	28.63	/	/	/
	2	5.194	18.01	3.47	0.0314	0.894	28.51	/	/	/
0.3 MPa	0.4	3.814	1.37	0.36	0.0710	-1.200	-16.90	5.94	83.63	0.1535
	0.5	4.304	3.14	0.73	0.0362	-0.737	-20.34	6.38	176.14	0.0631
	0.6	4.734	5.10	1.08	0.0273	-0.419	-15.36	7.70	281.98	0.0388
	0.7	5.108	7.50	1.47	0.0191	-0.201	-10.52	8.44	441.60	0.0259
	0.8	5.428	10.20	1.88	0.0154	-0.035	-2.30	10.25	666.45	0.0175
	0.9	5.691	12.29	2.16	0.0138	0.057	4.14	12.08	878.21	0.0134
	1	5.869	15.61	2.66	0.0115	0.114	9.94	13.42	1171.89	0.0104
	1.2	5.823	18.95	3.26	0.0099	0.1944	19.67	18.18	1840.12	0.0063
	1.5	5.579	19.85	3.56	0.0100	0.223	22.19	23.70	2362.09	0.0047
	2	5.202	18.20	3.50	0.0111	0.247	22.19	34.15	3068.58	0.0033
0.5 MPa	0.4	3.814	1.03	0.27	0.0591	-1.258	-21.28	4.09	69.27	0.2533
	0.5	4.305	2.12	0.49	0.0334	-0.741	-22.17	4.73	141.45	0.0979
	0.6	4.736	4.00	0.84	0.0201	-0.503	-25.00	5.46	271.25	0.0476
	0.7	5.116	6.00	1.17	0.0149	-0.239	-16.01	6.51	436.56	0.0299
	0.8	5.437	9.00	1.66	0.0109	-0.109	-9.99	6.98	640.77	0.0204
	0.9	5.403	11.36	2.10	0.0088	-0.012	-1.36	7.30	827.48	0.0144
	1	5.896	13.20	2.34	0.0085	0.024	2.77	9.11	1070.74	0.0116
	1.2	5.836	18.50	3.17	0.0074	0.095	12.79	12.07	1632.81	0.0073
	1.5	5.586	19.78	3.54	0.0069	0.125	18.14	15.00	2175.10	0.0052
	2	5.205	18.05	3.47	0.0085	0.152	17.79	20.88	2443.86	0.0043

**Table A3**  
Experimental data at 400 K.

	$\phi$	$\rho_u/\rho_b$	$Ss$ (m/s)	$u_l$ ( m/s)	$\delta_k$ (mm)	$L_b$ (mm)	$Ma_b$	$r_{cl}$ (mm)	$Pe_{cl}$	$K_{cl}$
0.1 MPa	0.4	3.512	2.39	0.68	0.1162	-1.075	-9.25	17.33	149.12	0.0554
	0.5	3.949	4.29	1.09	0.0753	-0.699	-9.28	20.99	278.93	0.0314
	0.6	4.329	7.77	1.80	0.0469	-0.372	-7.93	27.13	578.11	0.0157
	0.7	4.655	10.63	2.28	0.0380	-0.192	-5.05	36.26	953.56	0.0099
	0.8	4.925	13.70	2.78	0.0321	0.106	3.30	46.07	1433.39	0.0069
	0.9	5.135	15.68	3.05	0.0301	0.157	5.21	56.19	1865.27	0.0054
	1	5.269	18.56	3.52	0.0261	0.321	12.31	63.33	2427.49	0.0042
	1.2	5.259	20.01	3.81	0.0254	0.551	21.69	/	/	/
	1.5	5.065	21.98	4.34	0.0249	0.840	33.73	/	/	/
	2	4.744	20.05	4.23	0.0286	0.932	32.54	/	/	/
0.3 MPa	0.4	3.512	1.71	0.49	0.0583	-1.170	-20.08	6.95	119.27	0.0866
	0.5	3.949	3.44	0.87	0.0337	-0.710	-21.08	7.77	230.70	0.0417
	0.6	4.329	6.05	1.40	0.0217	-0.420	-19.37	8.58	396.08	0.0247
	0.7	4.655	9.01	1.94	0.0161	-0.172	-10.66	10.30	639.25	0.0158
	0.8	4.925	11.98	2.43	0.0132	-0.002	-0.18	12.10	916.48	0.0114
	0.9	5.135	14.35	2.80	0.0118	0.078	6.64	14.46	1223.62	0.0087
	1	5.269	16.90	3.21	0.0106	0.129	12.23	15.70	1484.12	0.0073
	1.2	5.300	19.82	3.74	0.0096	0.202	21.09	19.62	2052.66	0.0052
	1.5	5.087	21.40	4.21	0.0092	0.233	25.24	24.49	2657.34	0.0038
	2	4.753	19.94	4.20	0.0102	0.249	24.44	35.57	3490.04	0.0027
0.5 MPa	0.4	3.512	1.11	0.31	0.0563	-1.196	-21.25	4.37	77.60	0.1859
	0.5	3.951	3.10	0.78	0.0233	-0.736	-31.55	4.79	205.43	0.0573
	0.6	4.335	5.50	1.27	0.0149	-0.448	-30.07	5.77	387.42	0.0281
	0.7	4.670	7.70	1.65	0.0118	-0.217	-18.42	6.84	579.34	0.0192
	0.8	4.958	11.00	2.22	0.0090	-0.075	-8.35	7.40	819.53	0.0137
	0.9	5.197	13.50	2.60	0.0076	0.005	0.61	8.23	1077.10	0.0104
	1	5.360	16.50	3.08	0.0069	0.033	4.74	9.42	1369.30	0.0083
	1.2	5.314	19.22	3.62	0.0062	0.106	17.21	12.41	2011.95	0.0054
	1.5	5.095	21.094	4.14	0.0059	0.136	23.25	15.12	2576.57	0.0040
	2	4.756	19.229	4.04	0.0066	0.155	23.59	21.45	3263.69	0.0029

## References

- [1] Bradley D, Harper CM. The development of instabilities in laminar explosion flames. *Combust Flame* 1994;99(3–4):562–72.
- [2] Bechtold JK, Matalon M. Hydrodynamic and diffusion effects on the stability of spherically expanding flames. *Combust Flame* 1987;67(1):77–90.
- [3] Bradley D, Lawes M, Liao S, Saat A. Laminar mass burning and entrainment velocities and flame instabilities of *i*-octane, ethanol and hydrous ethanol/air aerosols. *Combust Flame* 2014;161(6):1620–32.
- [4] Nair A, Velamati RK, Kumar S. Effect of CO<sub>2</sub>/N<sub>2</sub> dilution on laminar burning velocity of liquid petroleum gas-air mixtures at elevated temperatures. *Energy* 2016;100:145–53.
- [5] Vu TM, Park J, Kim JS, Kwon OB, Yun JH, Keel SI. Experimental study on cellular instabilities in hydrocarbon/hydrogen/carbon monoxide–air premixed flames. *Int J Hydrogen Energy* 2011;36(11):6914–24.
- [6] Wu F, Jomaas G, Law CK. An experimental investigation on self-acceleration of cellular spherical flames. *Proc Combust Inst* 2013;34(1):937–45.
- [7] Aung KT, Hassan MI, Faeth GM. Flame stretch interactions of laminar premixed hydrogen/air flames at normal temperature and pressure. *Combust Flame* 1997;109(1–2):1–24.
- [8] Kwon OC, Faeth GM. Flame/stretch interactions of premixed hydrogen-fueled flames: measurements and predictions. *Combust Flame* 2001;124(4):590–610.
- [9] Kim W, Sato Y, Johzaki T, Endo T, Shimokuri D, Miyoshi A. Experimental study on self-acceleration in expanding spherical hydrogen-air flames. *Int J Hydrogen Energy* 2018;43(27):12556–64.
- [10] Beeckmann J, Hesse R, Kruse S, Berens A, Peters N, Pitsch H, et al. Propagation speed and stability of spherically expanding hydrogen/air flames: Experimental study and asymptotics. *Proc Combust Inst* 2017;36(1):1531–8.
- [11] Bradley D, Lawes M, Liu K, Verhelst S, Woolley R. Laminar burning velocities of lean hydrogen–air mixtures at pressures up to 1.0 MPa. *Combust Flame* 2007;149(1–2):162–72.
- [12] Hu E, Huang Z, He J, Miao H. Experimental and numerical study on lean premixed methane–hydrogen–air flames at elevated pressures and temperatures. *Int J Hydrogen Energy* 2009;34(16):6951–60.
- [13] Huo J, Saha A, Ren Z, Law CK. Self-acceleration and global pulsation in hydrodynamically unstable expanding laminar flames. *Combust Flame* 2018;194:419–25.
- [14] Huo J, Saha A, Shu T, Ren Z, Law CK. Self-acceleration and global pulsation in expanding laminar H<sub>2</sub>–O<sub>2</sub>–N<sub>2</sub> flames. *Phys Rev Fluids* 2019;4(4):043201.
- [15] Bradley D. Instabilities and flame speeds in large-scale premixed gaseous explosions. *Philosophical Transactions of the Royal Society of London. Series A: Mathematical, Physical and Engineering Sciences* 1999;357(1764):3567–81.
- [16] Law CK, Jomaas G, Bechtold JK. Cellular instabilities of expanding hydrogen/propane spherical flames at elevated pressures: theory and experiment. *Proc Combust Inst* 2005;30(1):159–67.
- [17] Kim WK, Mogi T, Kuwana K, Dobashi R. Prediction model for self-similar propagation and blast wave generation of premixed flames. *Int J Hydrogen Energy* 2015;40(34):11087–92.
- [18] Kwon OC, Rozenchan G, Law CK. Cellular instabilities and self-acceleration of outwardly propagating spherical flames. *Proc Combust Inst* 2002;29(2):1775–83.
- [19] Jomaas G, Law CK, Bechtold JK. On transition to cellularity in expanding spherical flames. *J Fluid Mech* 2007;583:1–26.
- [20] Bradley D, Lawes M, Mansour MS. Explosion bomb measurements of ethanol–air laminar gaseous flame characteristics at pressures up to 1.4 MPa. *Combust Flame* 2009;156(7):1462–70.
- [21] Bradley D, Hicks RA, Lawes M, Sheppard CGW, Woolley R. The measurement of laminar burning velocities and Markstein numbers for iso-octane–air and iso-octane–*n*-heptane–air mixtures at elevated temperatures and pressures in an explosion bomb. *Combust Flame* 1998;115(1–2):126–44.
- [22] Gu XJ, Haq MZ, Lawes M, Woolley R. Laminar burning velocity and Markstein lengths of methane–air mixtures. *Combust Flame* 2000;121(1–2):41–58.
- [23] Mannaa O, Mansour MS, Roberts WL, Chung SH. Laminar burning velocities at elevated pressures for gasoline and gasoline surrogates associated with RON. *Combust Flame* 2015;162(6):2311–21.
- [24] Kim W, Sato Y, Johzaki T, Endo T. Experimental study on the onset of flame acceleration due to cellular instabilities. *J Loss Prev Process Ind* 2019;60:264–8.
- [25] Bradley D, Lawes M, Morsy ME. Flame speed and particle image velocimetry measurements of laminar burning velocities and Markstein numbers of some hydrocarbons. *Fuel* 2019;243:423–32.
- [26] Bradley D, Lawes M, Mumby R, Ahmed P. The stability of laminar explosion flames. *Proc Combust Inst* 2019;37(2):1807–13.
- [27] Morsy ME, Yang J. Numerical and experimental study on turbulence statistics in a large fan-stirred combustion vessel. *Exp Fluids* 2021;62(5):1–20.
- [28] Bradley D, Lawes M, Morsy ME. Measurement of turbulence characteristics in a large scale fan-stirred spherical vessel. *J Turbul* 2019;20(3):195–213.
- [29] Lawes M, Sharpe GJ, Tripathi N, Cracknell RF. Influence of spark ignition in the determination of Markstein lengths using spherically expanding flames. *Fuel* 2016;186:579–86.
- [30] Kelley AP, Law CK. Nonlinear effects in the extraction of laminar flame speeds from expanding spherical flames. *Combust Flame* 2009;156(9):1844–51.
- [31] Morsy MEMH. Studies of laminar and turbulent combustion using particle image velocimetry. University of Leeds; 2019. PhD thesis.
- [32] Göttgens J, Mauss F, Peters N. Analytic approximations of burning velocities and flame thicknesses of lean hydrogen, methane, ethylene, ethane, acetylene, and propane flames. *Symp (Int) Combust* 1992;24(1):129–35.
- [33] Morley C. Gaseq: a chemical equilibrium program for Windows. Ver 2005:79.
- [34] Wu F, Liang W, Chen Z, Ju Y, Law CK. Uncertainty in stretch extrapolation of laminar flame speed from expanding spherical flames. *Proc Combust Inst* 2015;35(1):663–70.
- [35] Huo J, Yang S, Ren Z, Zhu D, Law CK. Uncertainty reduction in laminar flame speed extrapolation for expanding spherical flames. *Combust Flame* 2018;189:155–62.
- [36] Liang W, Wu F, Law CK. Extrapolation of laminar flame speeds from stretched flames: Role of finite flame thickness. *Proc Combust Inst* 2017;36(1):1137–43.
- [37] Mueller MA, Kim TJ, Yetter RA, Dryer FL. Flow reactor studies and kinetic modeling of the H<sub>2</sub>/O<sub>2</sub> reaction. *Int J Chem Kinet* 1999;31(2):113–25.
- [38] Konnov AA. Remaining uncertainties in the kinetic mechanism of hydrogen combustion. *Combust Flame* 2008;152(4):507–28.
- [39] Bauwens CRL, Berghthorson JM, Dorofeev SB. Experimental investigation of spherical-flame acceleration in lean hydrogen–air mixtures. *Int J Hydrogen Energy* 2017;42(11):7691–7.
- [40] Dayma G, Halter F, Dagaut P. New insights into the peculiar behavior of laminar burning velocities of hydrogen–air flames according to pressure and equivalence ratio. *Combust Flame* 2014;161(9):2235–41.
- [41] Verhelst S, Woolley R, Lawes M, Sierens R. Laminar and unstable burning velocities and Markstein lengths of hydrogen–air mixtures at engine-like conditions. *Proc Combust Inst* 2005;30(1):209–16.
- [42] Kuznetsov M, Kobelt S, Grune J, Jordan T. Flammability limits and laminar flame speed of hydrogen–air mixtures at sub-atmospheric pressures. *Int J Hydrogen Energy* 2012;37(22):17580–8.
- [43] Aung KT, Hassan MI, Faeth GM. Effects of pressure and nitrogen dilution on flame/stretch interactions of laminar premixed H<sub>2</sub>/O<sub>2</sub>/N<sub>2</sub> flames. *Combust Flame* 1998;112(1–2):1–15.
- [44] Alekseev VA, Christensen M, Konnov AA. The effect of temperature on the adiabatic burning velocities of diluted hydrogen flames: A kinetic study using an updated mechanism. *Combust Flame* 2015;162(5):1884–98.
- [45] Kitagawa T, Nakahara T, Maruyama K, Kado K, Hayakawa A, Kobayashi S. Turbulent burning velocity of hydrogen–air premixed propagating flames at elevated pressures. *Int J Hydrogen Energy* 2008;33(20):5842–9.
- [46] Smith GP, Golden DM, Frenklach M, Moriarty NW, Eiteneer B, Goldenberg M, Bowma CT, Hanson RK, Song S, Gardiner Jr WC, Lissianski, VV. GRI 3.0 Mechanism. Gas Research Institute ([http://www.me.berkeley.edu/gri\\_mech](http://www.me.berkeley.edu/gri_mech)) (accessed December 2021).
- [47] ANSYS CHEMKIN 19.1. ANSYS Reaction Design: San Diego. 2019.
- [48] Taylor SC. Burning velocity and the influence of flame stretch. Leeds University; 1990. Ph.D. Thesis.
- [49] Sun ZY, Li GX. Propagation characteristics of laminar spherical flames within homogeneous hydrogen–air mixtures. *Energy* 2016;116:116–27.
- [50] Oppong F, Zhongyang L, Li X, Xu C. Inherent instabilities in ethyl acetate premixed flames. *Fuel* 2021;290:120000.
- [51] Bradley D, Lawes M, Morsy ME. Combustion-induced turbulent flow fields in premixed flames. *Fuel* 2021;290:119972.